J. Fluid Mech. (2013), *vol.* 736, *pp.* 44–66.
doi:10.1017/jfm.2013.525

Thermodynamic effects during growth and collapse of a single cavitation bubble

Matevž Dular[1],† **and Olivier Coutier-Delgosha**[2]

[1]Laboratory for Water and Turbine Machines, University of Ljubljana, Aškerčeva 6, 1000 Ljubljana, Slovenia

[2]LML Laboratory, Arts et Metiers ParisTech, 8 Boulevard Louis XIV, 59046 Lille, France

(Received 4 December 2012; revised 26 August 2013; accepted 1 October 2013; first published online 1 November 2013)

The thermodynamic effects associated with the growth and collapse of a single cavitation bubble are investigated in the present paper by an experimental approach. The study focuses on the temperature variations in the liquid surrounding the bubble. Experiments are conducted in a cylinder partially filled with water at an ambient temperature and atmospheric pressure. The bubble growth results from the expansion of an initial air bubble, due to the pressure wave generated by a so-called 'tube-arrest' method. Several locations of the bubble, at different distances from the bottom wall of the cylinder, are considered. The bottom wall is made of sapphire, which is transparent to both the visible and infrared light spectra which enables temperature measurements by a high-speed thermovision camera at a wavelength of 3–5 μm. Water is opaque to the infrared light spectrum, hence only temperatures in the boundary layer and on the liquid vapour interface could be determined. A temperature decrease of ∼3 K was recorded during the bubble growth while an increase up to 4 K was detected during the collapse. Experimental results are compared to the predictions of the 'thermal delay' model based on the assumption that the bubble growth and collapse are due to phase changes only. In this approach, the temperature variations are related to the latent heat exchanges during the vapourization and condensation processes. On the basis of these results, the respective effects of phase change and air dilatation/compression in the bubble dynamics are discussed.

Key words: cavitation, drops and bubbles, phase change

1. Introduction

Cavitation is a phenomenon characterized by vapour generation and condensation in high-speed liquid flows. It frequently occurs in industrial configurations such as rotating machinery, injectors, and other hydraulic devices. Most of the time it is accompanied by effects like vibrations, increase of hydrodynamic drag, changes in the flow hydrodynamics, noise, erosion, light effects such as sonoluminescence, and also thermal effects. The thermal effects are usually neglected, since the influence of the temperature variations on the integral flow properties is small in common liquids such as cold water (Hord, Anderson & Hall 1972). However, on the local scale each individual bubble undergoes a considerable rise of temperature during the collapse

† Email address for correspondence: matevz.dular@fs.uni-lj.si

(Hauke, Fuster & Dopazo 2007), while significant local cooling of the liquid is also expected within the cavitation areas (Franc, Rebattet & Coukon 2004).

Cavitation is usually initiated by a local pressure drop in the vicinity of a cavitation nucleus. As the bubble grows, latent heat is supplied from the surrounding liquid to the interface, creating a thermal boundary layer. The consequence is a small local decrease of the liquid temperature, which results in a slight drop of the vapour pressure. This delays the further development of the bubble, because a greater pressure drop is needed to maintain the process. This phenomenon is known as 'thermal delay', as it plays a moderating role in the development of cavitation (Brennen 1995).

Thermodynamic effects can usually be neglected in fluids for which the critical-point temperature is much higher than the working temperature. On the other hand, the effects become significant when the critical-point temperature is close to the temperature of the fluid, as in the case of cryogenic fluids (Stahl & Stepanoff 1956). Therefore, the understanding and the prediction of the thermodynamic effect is crucial in many applications; for example the turbopumps for liquid hydrogen LH2 and oxygen LOx in space launcher engines need to have an inducer rotor installed upstream from the main impellers, in order to achieve high suction performance. The inducer is designed to operate in moderate cavitating conditions, hence a minimum pressure level in the tanks must be ensured, in order to avoid the occurrence of large sheet cavities on the blades, which are often associated with large-scale instabilities. Particularity well known is the failure of the Japanese H-II rocket due to rotating cavitation in the LH2 turbopump (Sekita *et al.* 2001). To avoid such risk the pressure in the tanks, and thus their structure and weight, cannot be reduced, which is one of the fundamental limitations on the increase of the useful mass carried by the launcher.

The thermodynamic effect is favourable when pumping cryogenic fluids as it delays the cavitation development in the cavitation area. Hence, the rocket engine turbopump inducer, at given suction pressure, performs better than predicted without consideration of thermal effects. However the degree of improvement depends on the strength of the thermodynamic effect, which can at present only be roughly estimated, for example by the thermodynamic parameter proposed by Brennen (1995).

Past studies have mostly concentrated on the consequences of the thermodynamic effect rather than on the investigation of the mechanism itself. For example, its amplitude has been estimated mainly by comparison between the cavitation development: (i) in a liquid characterized by a large thermodynamic effect; and (ii) in a liquid with negligible thermodynamic effect.

The first study on the thermodynamic effect was conducted by Stahl & Stepanoff (1956), who investigated its consequence on pump performance. In the same period, Sarosdy & Acosta (1961) reported differences in the appearance of cavitation in water and Freon-113. Quantitative estimations of the thermodynamic effects were first proposed by Ruggeri & Moore (1969) who measured the variations of pump performance for various temperatures and fluids. Probably the most thorough experimental set of data on cryogenic cavitation in Venturi sections, hydrofoil sections and ogives was published by Hord *et al.* (1972) and Hord (1973*a*,*b*); it is still considered as a benchmark for validating models of thermodynamic effects in cavitation. More recent studies have focused on the influence of the thermodynamic effect of cavitation on performance and cavitation instabilities in rotating machinery such as turbopump inducers used for rocket propulsion. Franc *et al.* (2004) conducted experiments both with water and refrigerant R114 to analyse the modifications of the cavitation instabilities, and a similar study was also conducted by Cervone, Testa & d'Agostino (2005) with hot and cold water at 343 and 293 K, respectively.

In these experimental investigations, temperature variations themselves are rarely considered: one example is Fruman, Reboud & Stutz (1999) who measured the local wall temperature under the cavity with five micro-thermocouples. More recently, on-board measurements of temperature depression within the sheet cavity at the leading edge of inducer blades were also recorded (Franc *et al.* 2010). Time-averaged temperature variations and characteristic fluctuation frequencies related to cavitation instabilities have been analysed.

Probably owing to the complexity of the experimental investigations, the thermodynamic effects are nowadays usually estimated by rudimentary models, most of them proposed between 1960 and 1990. The most commonly used parameters in these approaches are the non-dimensional B-factor, which is a dimensionless temperature depression (Stepanoff 1961), and dimensional parameters like Σ (Brennen 1973), α (Kato 1984) or Σ^* (Watanabe *et al.* 2007).

To improve the prediction of the thermal delay, modelling of the heat transfers associated with phase change needs to be improved. This requires experimental investigations of the temperature variations in the liquid, due to vapourization and condensation. Although a vast number of experimental studies of thermodynamic effects in cavitation flow exist, almost none of them deals with the effect directly. It is therefore essential to develop a technique that would enable direct measurements of temperatures in cavitating flow.

The present study is devoted to the first direct measurements of the thermodynamic effect. The analysis is focused on a single vapour bubble evolution. To initiate the bubble growth, a so-called tube-arrest method is used (Chesterman 1952). It is particularly suited for the present measurements since it does not introduce thermal energy from an outside source to create a bubble; for example measurements where the bubble was created by laser light or by electric discharge would be meaningless as thermal energy would be transferred to the liquid and thus modify significantly the local temperature. A non-invasive high-speed thermographic method was applied to measure the temperature field in the liquid close to the bubble interface during its successive growth and collapse. In addition, two conventional high-speed cameras were used to simultaneously observe the bubble shape evolution. Experimental results were, finally, compared to calculations based on the theories of bubble dynamics and the thermal delay.

2. Theoretical background

A theoretical approach to the process of bubble expansion and implosion, which is investigated here, can be found for example in Brennen (1995) or Franc & Michel (2004). When the pressure drops, the bubble begins to grow due to both water evaporation and gas expansion, i.e. expansion of the air contained inside the initial nucleus. During the collapse, the process is reversed: the main mechanisms are now condensation of vapour and compression of gases. In both phenomena, the magnitude of temperature variations in the thermal layer around the bubble depends strongly on the predominant process that drives the bubble size evolution: gas expansion/compression and the phase changes (Toegel *et al.* 2000; Matula *et al.* 2002).

2.1. *Isothermal or adiabatic process*

To estimate which of the processes is dominant (expansion/compression or vapourization/condensation), the energy balance of the gas inside the bubble is written

as follows, where it is assumed that the initial bubble undergoes a pressure drop in time Δt during which the radius grows from R up to $R + \Delta R$ and the gas temperature changes by ΔT:

$$(\tfrac{4}{3}\pi R^3)\rho_g c_{vg}\Delta T = \Delta Q - p(4\pi R^2 \Delta R), \tag{2.1}$$

where ρ_g and c_{vg} are the density and the specific heat at constant volume of the gas, ΔQ is the heat received by the bubble from the liquid, and p is the pressure at the bubble interface. So, the left-hand side term stands for the variation of internal energy of the gas during the time Δt, while the second term on the right-hand side is the work of the pressure force at the bubble surface (as in many past studies, such as Yasui 1997; Storey & Szeri 2001; Szeri *et al.* 2003, the terms for kinetic energy, the energy of bubble deformation etc. are neglected in (2.1)).

Because of the temperature variation within the gas, a thermal boundary layer develops in the liquid around the bubble. Its thickness is of the order of $\sqrt{\alpha_l \Delta t}$ (Franc *et al.* 2004), with α_l the thermal diffusivity in the liquid. The temperature gradient in this boundary layer induces heat transfer by conduction, which drives the heat ΔQ to the bubble.

Fourier's law in the thermal layer can be written as follows:

$$\Delta Q \approx -\lambda_l \frac{\Delta T}{\sqrt{\alpha_l \Delta t}} 4\pi R^2 \Delta t = -\sqrt{\lambda_l \rho_l c_{pl}}\sqrt{\Delta t} 4\pi R^2 \Delta T, \tag{2.2}$$

where $\alpha_l = \lambda_l/\rho_l c_{pl}$ with λ_l the thermal conductivity in the liquid, ρ_l the liquid density, and c_{pl} the heat capacity at constant pressure in the liquid.

The energy balance equation (2.1) allows an estimation of the temperature variation of the gas in the bubble:

$$\Delta T \approx \frac{\Delta T_{ad.}}{1 + \sqrt{\dfrac{\Delta t}{\Delta t_r}}}, \tag{2.3}$$

where the particular adiabatic case ($\Delta Q = 0$) leads to $\Delta T_{ad.} = -3(p\Delta R/\rho_g c_{vg} R)$. If we assume that the temperature variation inside the bubble is entirely due to the heat exchanges ($p(4\pi R^2 \Delta R) = 0$ which results in $(4\pi R^3/3)\rho_g c_{vg}\Delta T = \Delta Q$ for (2.1)) and combine this expression with (2.2) we get Δt_r which is the characteristic time of the heat transfer process at the bubble interface:

$$\Delta t_r = \frac{(\rho_g c_{vg} R)^2}{9\lambda_l \rho_l c_{pl}}. \tag{2.4}$$

The process can be considered adiabatic if the bubble lifetime is much shorter that the characteristic time of heat transfer Δt_r; the bubble evolution is then mainly driven by expansion and compression of gases. In the opposite case, if there is enough time for the heat transfer to proceed until thermal equilibrium is reached ($\Delta t_r \ll \Delta t$), the process is closer to isothermal conditions ((2.3) gives $\Delta T = 0$), which means that evaporation and condensation of water and water vapour are the main driving mechanisms.

In the present experiments, a typical bubble in water at 20°C grew and collapsed in ∼16 ms and its maximum radius was close to 9 mm (see for example figure 8). Considering (2.4) with $\rho_l = 999$ kg m^{-3}, $\rho_g = 0.0173$ kg m^{-3}, $c_{pl} = 4182$ J kg^{-1} K^{-1}, $c_{vg} = 717$ J kg^{-1} K^{-1} and $\lambda_l = 0.653$ W m^{-1} K^{-1}, then $\Delta t_r \approx 0.5$ ns is obtained. The characteristic time of heat transfer (0.5 ns) is much smaller than the bubble

lifetime (16 ms), which means that mass transfer (evaporation and condensation) takes place and can be considered as the main reason for the measured temperature variations. Expansion and compression may only occur at the very beginning of bubble growth and just before it collapses to its minimum size, which also complies with the findings of Akhatov *et al.* (2001) who predicted these two processes to be dominant only during the first/last few per cent of bubble life. Therefore, the thermal delay theory can be applied to interpret the results of the present measurements.

2.2. *Thermal delay*

The notion of thermal delay can be most simply presented in the case of a spherical bubble in infinite liquid. As the pressure at infinity drops, an initial spherical nucleus begins to grow and becomes a much larger bubble. The evaporation process involved in this growth requires the latent heat L to be supplied by the liquid at the bubble interface. In the case of an isolated bubble, an estimation of the heat flux transferred from the liquid to the gas can be obtained from Fourier's law in (2.2), using the order of magnitude of the thermal boundary layer $\sqrt{\alpha_l \Delta t}$:

$$q = \frac{\Delta Q}{4\pi R^2 \Delta t} \approx -\lambda_l \frac{T_b - T_\infty}{\sqrt{\alpha_l \Delta t}}, \tag{2.5}$$

where q is the heat flux per unit surface, T_b is the liquid temperature at the bubble interface, and T_∞ is the ambient liquid temperature. Assuming that the bubble size evolution is entirely due to vapourization or condensation, the energy balance equation can be written as:

$$q = \rho_l L \dot{R}, \tag{2.6}$$

where $\dot{R}$ is the growth rate of the bubble, which gives an estimation for the temperature difference:

$$T_b - T_\infty = -\frac{\dot{R}\sqrt{t}}{\sqrt{\alpha_l}} \frac{\rho_v L}{\rho_l c_{pl}}. \tag{2.7}$$

If we further simplify the analysis by neglecting the initial size of the nucleus and assuming that the growth velocity of the bubble is of the order of $R/\Delta t$ (see Brennen 1995) we get:

$$T_b - T_\infty = -\frac{R}{\sqrt{\alpha_l \Delta t}} \frac{\rho_v L}{\rho_l c_{pl}}. \tag{2.8}$$

Equation (2.8) provides an order of magnitude of the temperature difference expected in the liquid close to the bubble interface. For the present study, water at 20 ∘ C was used, and the bubble grew to a radius of ∼9 mm in approximately 10 ms. With $\rho_l = 999$ kg m^{-3}, $\rho_v = 0.0173$ kg m^{-3}, $c_{pl} = 4182$ J kg^{-1} K^{-1}, $\lambda_l = 0.653$ W m^{-1} K^{-1}, $L = 2454.3$ kJ kg^{-1} and $\alpha_l = \lambda_l/\rho_l c_{pl} = 1.56 \times 10^{-7}$ m^2 s^{-1}, a cooling of ∼2.3 K is obtained.

Heat transfer from the liquid to the bubble is possible only if the temperature T_b inside the bubble is smaller than T_∞. Hence, the vapour pressure inside the bubble $p_v(T_b)$ is also smaller than its value $p_v(T_\infty)$ in the liquid bulk. Consequently, the pressure imbalance between the bubble and the reference point at infinity $p_v(T_\infty) - p_v(T_b)$ increases, so that the growth rate of the bubble is reduced. To estimate this variation of vapour pressure, the following equation is based on the Clapeyron

relation where the vapour density is neglected compared to the liquid one:

$$L = T\left[\frac{1}{\rho_v} - \frac{1}{\rho_l}\right]\frac{\mathrm{d}p_v}{\mathrm{d}T} \approx \frac{T}{\rho_v}\frac{\mathrm{d}p_v}{\mathrm{d}T}. \tag{2.9}$$

The thermodynamic effect in terms of vapour pressure difference can thus be expressed as:

$$\Delta p_v = p_v(T_\infty) - p_v(T_b) \approx \frac{\mathrm{d}p_v}{\mathrm{d}T}\Delta T \approx \frac{\rho_v L \Delta T}{T_\infty}. \tag{2.10}$$

Combination of (2.8) and (2.10) finally leads to:

$$\Delta p_v = \frac{R}{\sqrt{\alpha_l \Delta t}}\frac{(\rho_v L)^2}{\rho_l c_{pl} T_\infty}, \tag{2.11}$$

which gives the decrease of the vapour pressure in the vicinity of the bubble due to the latent heat flow. The last equation, (2.11), will be used in § 4 together with Brennen's Σ parameter (Brennen 1995) to model the spherical bubble dynamics and the temperature at the interface.

3. Experiments

One of the simplest ways of creating a single cavitation bubble is the so-called tube-arrest method, which was first used by Chesterman (1952). The technique is based on a vertically mounted cylindrical tube containing liquid which is pulled downwards against tensioned supports and released. After the tube's arrest the liquid continues its upward motion generating a tension pulse, *ab initio*.

The experimental arrangement is shown in figure 1 and is for the most part the same as the one used by Chen & Wang (2004) in their experiments. A vertical acrylic glass tube (1) with inner diameter of 30 mm is open at the upper end. It is put into slides (2) so it can move freely in the vertical direction. The tube is 1 m long and filled with water up to the 700 mm level. Distilled water was used. In addition it was boiled for 10 min and cooled down to ambient temperature prior to the experiments to remove as many cavitation nuclei as possible.

The tube is fastened indirectly to a spring (3) pinned at one end. For the generation of a cavitation bubble, the tube is pulled downward for some specified length, the spring thus being compressed. The former is then released, and is quickly pushed upward by the spring, and then suddenly arrested by a barrier (4) after shooting up the short distance.

A thin rod (5) with a diameter of 2 mm was inserted vertically into the water. In the bottom part it had a small dent so that a small air bubble with a radius of 0.5 mm could be positioned within it (the bubble served as an artificial cavitation nucleus). The rod was suspended along the centreline of the tube.

During the sudden arrest, a tension wave is produced in the water column, starting from the tube bottom and travelling upward. The bottom of the tube is closed by an observation window (6) made out of sapphire glass which is transparent in both the visible and infrared light spectra. Two high-speed conventional black-and-white cameras recorded from the side and bottom views, while a high-speed IR camera was used to measure temperatures from the bottom (through the sapphire glass window).

The velocity V_s at which the tube was suddenly stopped was varied from 0.5 to 2 m s^{-1}. For that purpose, the tube displacement was set to $\sim$10 mm. These conditions lead to spherical growth of the bubble, with a maximal diameter of $\sim$20 mm reached

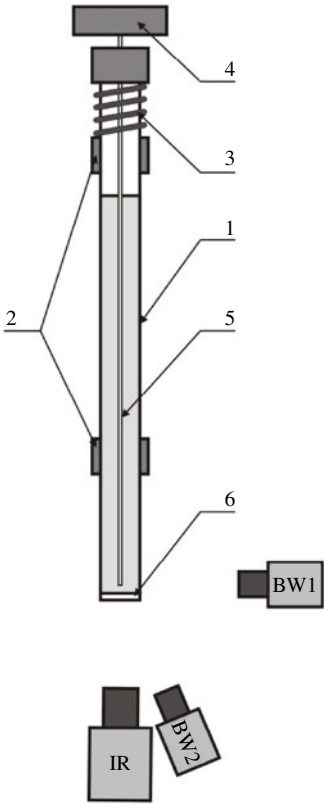

FIGURE 1. Experimental setup for creating a single cavitation bubble by a tube arrest method. For a description of the parts see the text.

in a time Δt close to 10 ms. Owing to the vicinity of the bottom wall there was a tendency of the bubble to form a micro-jet and to collapse asymmetrically (Philipp & Lauterborn 1998). The extent of asymmetry depended on the initial distance of the nucleus from the wall. The bubble position is commonly defined by the non-dimensional distance between the wall and the bubble:

$$\chi = \frac{h}{R_{max}}, \tag{3.1}$$

where R_{max} is the maximal bubble radius and h is the distance of the bubble centre from the wall: for $\chi > 1$, the bubble does not touch the wall, for $\chi = 1$, the bubble just touches the wall, and for $\chi < 1$, the bubble is in contact with the wall during some period of time.

Observation of the bubble was performed with two high-speed cameras: Fastec Imaging HiSpec4 2G mono and Motion Blitz EoSens mini 1, which captured images from side and bottom views, respectively. The cameras could capture images at 523 f.p.s. at 3 Mpixel and 506 f.p.s. at 1 Mpixel resolution, respectively. For the present experiments, the cameras were synchronized and recorded at 6000 f.p.s. at a reduced resolution. Figure 2 shows visualizations of bubble growth and collapse in three different configurations. In the first case, (*a*), $\chi = 0$ (the bubble is in contact with the wall during its whole lifetime); in the second case, (*b*), $\chi = 0.8$ (the bubble

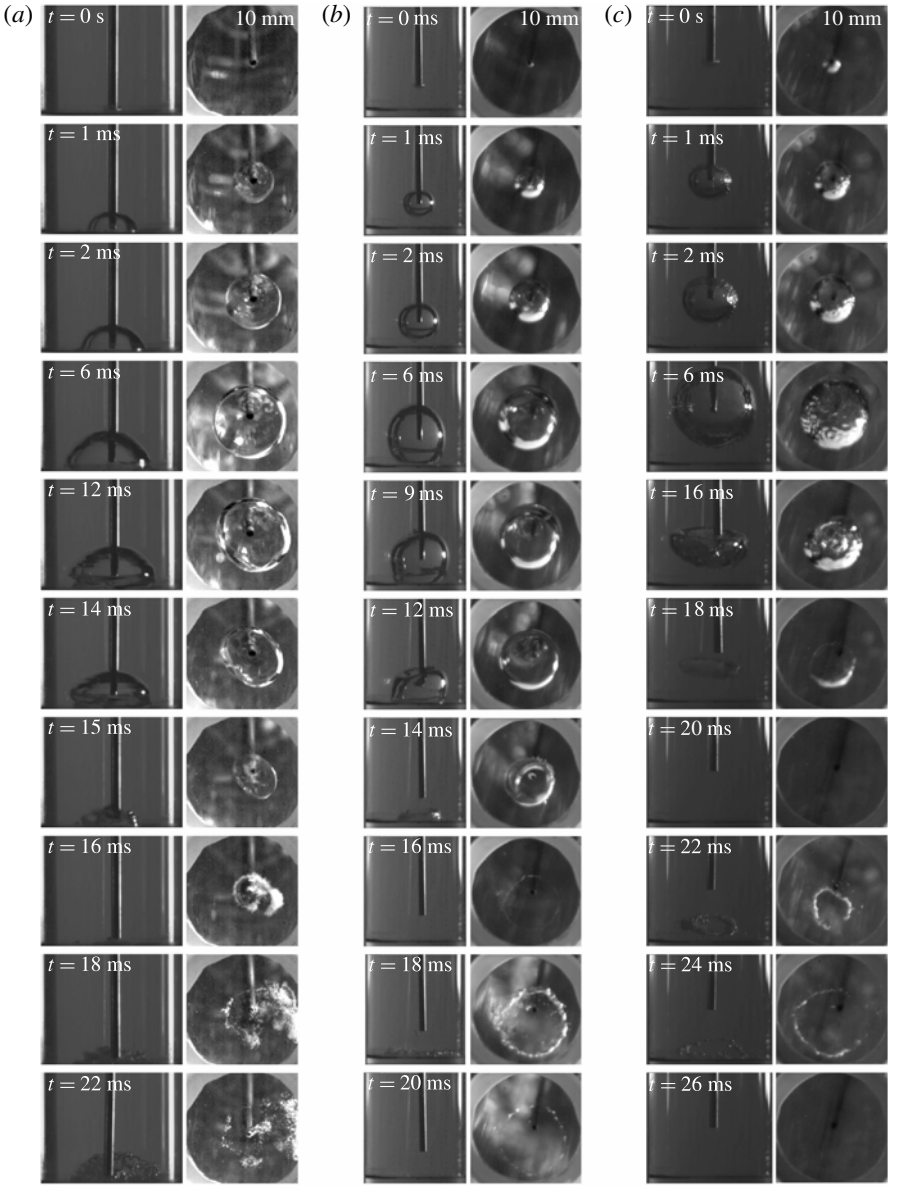

FIGURE 2. Visualization of bubble growth and collapse for non-dimensional standoff distances(*a*) $\chi = 0$, (*b*) $\chi = 0.8$ and (*c*)$\chi = 1.3$. Side view on the left and bottom view on the right.

is away from the wall at the beginning, but in contact later on); in the last case, (*c*), $\chi = 1.3$ (the bubble is never in contact with the wall).

It can be observed that the collapse of all three bubbles is strongly driven by the micro-jet (Plesset & Chapman 1971): due to the vicinity of the bottom the bubble becomes asymmetrical and a liquid jet penetrates it (particularly well seen at $t = 12$ ms for $\chi = 0.8$ and at $t = 16$ ms for $\chi = 1.3$). Also in all three cases, the rebound or splashing can be seen after the collapse (a torus of micro-bubbles nicely captured by the bottom view camera at $t = 18$ ms for $\chi = 0.8$ and at $t = 22$ ms

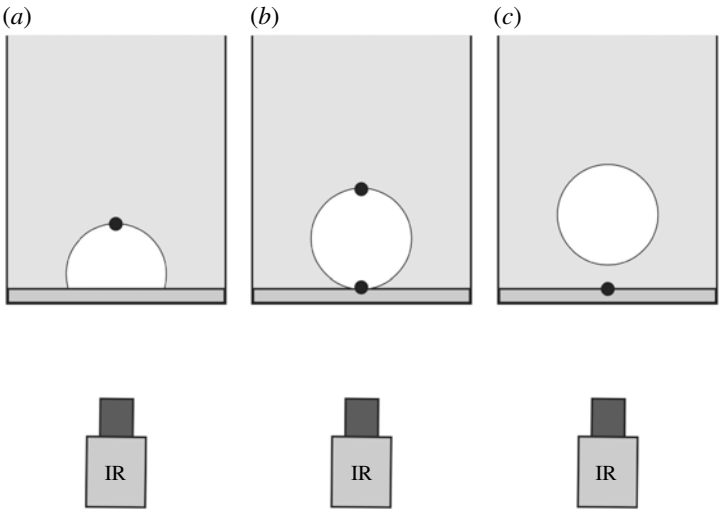

FIGURE 3. Localization of temperature measurements (black circle) for (*a*) $\chi < 1$, (*b*) $\chi = 1$ and (*c*) $\chi > 1$.

for $\chi = 1.3$). This is caused by the radial flow of the micro-jet which induces secondary evaporation (Tong *et al.* 1999).

In the case $\chi = 0$ (figure 2*a*), the shape of the bubble is half-spherical during most of its lifetime; only at the very end of the collapse, at $t = 15$ ms, does the bubble shape become severely distorted. In the case $\chi = 0.8$ (figure 2*b*), the bubble is initially spherical but the shape becomes asymmetrical when it contacts the wall at $t = 6$ ms, and a very distinctive micro-jet forms during the collapse (at $t = 12$ ms). In the final case $\chi = 1.3$ (figure 2*c*), the bubble grows and collapses far from the wall. The growth is therefore spherical, apart from the high mode instability, small distortions of the interface (Chen & Wang 2005). The collapse however is still significantly influenced by the vicinity of the wall and a micro-jet clearly occurs even in this case (at $t = 16$ ms).

In the three configurations, the evolution of the temperature field is investigated with a high-speed thermovision camera CMT384SM – Thermosensorik. Its sensitive wavelength range lies between 3 and 5 μm. It should be recalled that water has very specific properties regarding the propagation of infrared light – even a very thin layer of liquid (10 μm or even less) is absolutely opaque to the whole range of the infrared spectrum (Hale & Querry 1973). This implies that the thermal camera, in configuration $\chi > 1$, systematically records the temperature at the boundary between the sapphire glass and water. In case the $\chi = 1$, it is expected that this temperature is almost that of the liquid/vapour interface, at the bottom and/or upper point of the bubble, since vapour is transparent to infrared light. In the case $\chi < 1$, when the bubble is attached to the glass, the recorded temperature is that of the bubble interface at the upper part of the bubble, for the same reason (figure 3).

The opacity of water makes it appropriate for investigation of the thermodynamic effect in the present configuration. Indeed, if a transparent or semitransparent liquid were used, interpretation of the images would be more complex.

Two different acquisition frequencies were applied during the experiments. At a low frequency of 600 f.p.s. (i.e. 1/10th of the frame rate of the two conventional cameras), the main features of temperature variations were obtained with a sufficient

time resolution of the images to analyse the dynamics of the temperature field. The frame size at this frequency was 128×128 pixels and the integration time was 500 μs (one pixel corresponded roughly to 0.2 mm × 0.2 mm area). At a higher frequency (3840 f.p.s.) the frame size had to be reduced down to 32×32 pixels with the integration time of only 40 μs. This setting enabled better temporal resolution of the measurements, which enabled a more accurate comparison with the thermal delay theory.

The camera was calibrated in-situ. Uncertainty of the mean operating temperature of water was checked by comparison with measurements by an A-class Pt100 sensor and a discrepancy of ±0.2 K was found. However, our main goal was to quantify relative differences in the non-uniform time-dependent temperature field. For a single element on the temperature sensor of the thermocamera, the noise equivalent temperature difference (NETD) is less than 30 mK.

To test the repeatability of the installation (generation of the bubble and its temperature response) we generated four bubbles at the same conditions at a non-dimensional standoff distance $\chi = 0.8$. The results are shown in figures 8 and 9 in § 5. The differences in the size of the bubble are insignificant (figure 8*b* at $\chi = 0.8$), while somewhat larger discrepancies between the test runs are observed in the temperature evolution (figure 9*b* at $\chi = 0.8$). Nevertheless one can still claim that the measurements are repeatable.

4. Modelling

For further analysis of the experimental data, and discussion of the mechanisms that drive the temperature variations, comparison of the experimental time evolutions of the temperature with results of modelling is required. In the theoretical model we assume the bubble to remain spherical, which means that the influence of the bottom wall is neglected. The Rayleigh–Plesset equation (Plesset 1949) including thermal effects is considered:

$$\rho_l \left(R\ddot{R} + \frac{3}{2}\dot{R}^2 \right) = p_v(T_b) - p_\infty + p_{g0}\left(\frac{R_0}{R}\right)^{3\gamma} - \frac{2S}{R} - 4\mu\frac{\dot{R}}{R}. \tag{4.1}$$

Equation (4.1) can be rewritten as follows:

$$\rho_l \left(R\ddot{R} + \frac{3}{2}\dot{R}^2 \right) + \Delta p_v = p_v(T_\infty) - p_\infty + p_{g0}\left(\frac{R_0}{R}\right)^{3\gamma} - \frac{2S}{R} - 4\mu\frac{\dot{R}}{R}. \tag{4.2}$$

Considering (2.11) and introducing the parameter Σ (Brennen 1995) defined by $\Sigma = (\rho_v L)^2/\rho_l^2 c_{pl} T_\infty \sqrt{\alpha_l}$, the term Δp_v can be written as $\Delta p_v = \Sigma \dot{R}\sqrt{t}\rho_l$ which finally leads to:

$$\rho_l \left(R\ddot{R} + \frac{3}{2}\dot{R}^2 \right) + \Sigma \dot{R}\sqrt{t}\rho_l = p_v(T_\infty) - p_\infty + p_{g0}\left(\frac{R_0}{R}\right)^{3\gamma} - \frac{2S}{R} - 4\mu\frac{\dot{R}}{R}, \tag{4.3}$$

which gives the bubble radius evolution according to time t. It should be noted that other approaches for calculation of bubble size evolution in tubes exist (for example Chen & Wang 2005). However, although their approach works well for bubbles with size comparable to the tube size, the bubble evolution in the initial and final stages is not correctly predicted. As the velocity of the interface in these periods is of primary importance for the calculation of the thermodynamic effect, such a model is not suitable in the present study.

In § 5, (4.3) is solved numerically to obtain the bubble radius evolution as a function of time. Then (2.8) is applied to calculate the time evolution of the temperature T_b. Results are compared to the results of experimental measurements.

5. Results

The present section focuses on the analysis of the temperature measurements during the growth and collapse of the bubble. First, the data recorded with a low frame rate (600 f.p.s.) are shown and discussed. Then, measurements with the higher frame rate (3840 f.p.s.) are compared to the results of the Rayleigh–Plesset and thermal delay model to clarify the understanding of the experimental visualizations.

5.1. *Temperature measurements*

Figures 4–6 show (for the three experimental test cases: non-dimensional standoff distance $\chi = 0.8$, $\chi = 1$ and $\chi = 1.3$) five successive characteristic situations observed during the bubble lifetime. For each situation, the bottom and side views of the bubble are displayed together with the corresponding temperature field. In the three cases, time $t = 0$ corresponds to the bubble inception.

According to (2.8), cooling of the liquid due to the transfer of latent heat during the evaporation process should occur in the initial stage of the experiment. The case $\chi = 0$ (figure 4) leads to the simplest analysis, as the bubble is attached to the glass surface during the whole duration of the experiment. This condition enables continuous measurements of the temperature at the bubble surface (see figure 3*a*).

The cooling is observed slightly after the beginning of the bubble growth. The maximum temperature drop ΔT during the evaporation stage is $\sim$2 K. As the growth of the bubble decelerates the temperatures starts to grow. The rate of temperature increase is slow at first, but it is significantly accelerated as the cavity collapses at $t = 16$ ms in the form of a micro-jet. The acquired temperature field at the instant of bubble collapse should represent the temperature elevation of the liquid micro-jet, which is of the order of 3 K. This temperature increase may be due to the transfer of latent heat during the vapour condensation, and/or to the heat transfer between the vapour, whose temperature increases drastically during the gas compression, and the liquid micro-jet that flows through the bubble. Indeed, temperature elevations of several thousands Kelvin may occur in the vapour during a very short period of time at the end of the bubble collapse (Brennen 1995). However, such high values apply only to spherical collapse of bubbles, which is not the case in the present study.

After the bubble collapse, the heat is convected and diffused over the whole observation window, so the liquid temperature increases slightly (the change between the initial and final temperatures is 0.3 K) and no temperature deviation is recorded during the secondary evaporation observed by conventional cameras at $t = 18$ ms.

At a bigger standoff distance $\chi = 0.8$ (figure 5), the evolution is similar, but the temperature decrease is detected much later in the bubble lifetime, $\sim$6 ms after the start of the evaporation, which corresponds to the moment when the bubble contacts the wall. A maximum temperature drop of 1.2 K is obtained. The smaller temperature change in this configuration is a result of delayed acquisition of the temperature field as the opacity of water in the IR spectrum does not enable detection of the temperature variations associated with the first stage of bubble growth, before it reaches the wall. At $t = 14$ ms the bubble collapses in the form of a micro-jet. The acquired temperature field at this time ($t = 14$ ms) represents the temperature of the liquid micro-jet in the centre, which has been slightly increased by flowing through the vapour bubble that surrounds the jet. The temperature of the jet is $\sim$1.2 K above the

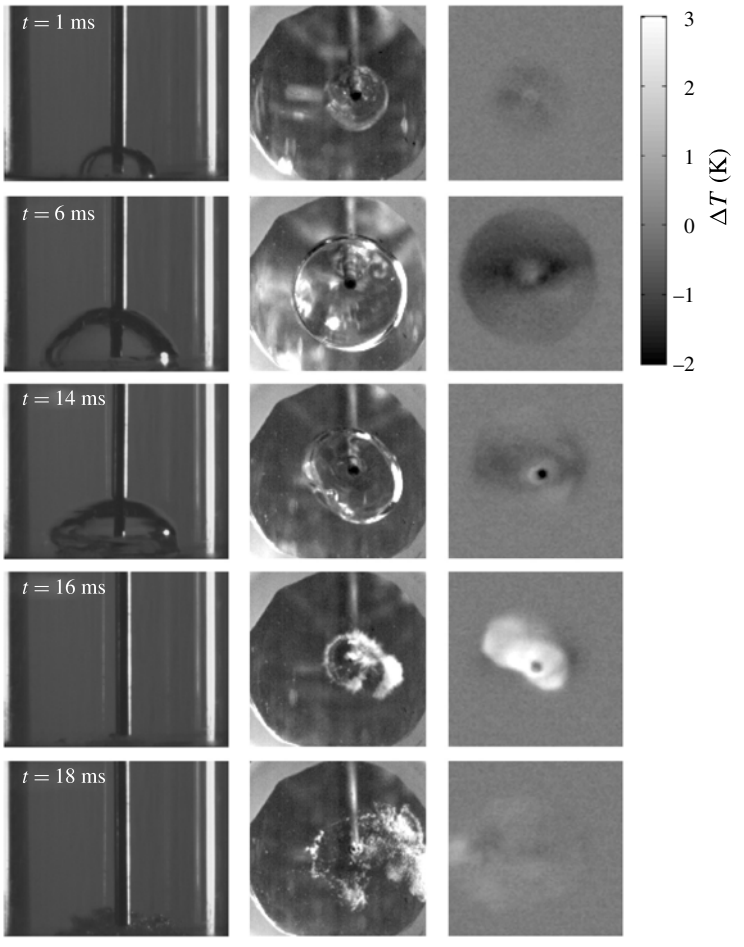

FIGURE 4. Evolutions of the bubble shape and temperature field for the case $\chi = 0$.

initial one. After the collapse the heat is again convected and diffused over the whole observation window. However, the change in liquid temperature is $\Delta T = 0.7$ K, which is larger than in the previous case at $\chi = 0$.

In the third case displayed in figure 6 ($\chi = 1.3$), the bubble never touches the sapphire window, so no cooling is detected (because of the water opacity in the IR spectrum). However, a 'hot spot' ($\sim$0.8 K of temperature increase) appears 18 ms after the bubble started to grow. It can be presumed that this local temperature elevation is associated with the micro-jet that hits the glass surface. Like in previous cases the final temperature is slightly higher than the initial one ($\Delta T = 1$ K).

It seems that the change between the initial and final temperature is dependent on the bubble standoff distance. This may be due to variations of the maximum temperature reached by the vapour during the final stage of the collapse (a bubble which is further from the wall collapses in more spherical shape which initiates higher gas temperatures) and also the difference in the jet velocity as it hits the window (according Plesset & Chapman 1971 it increases with the standoff distance).

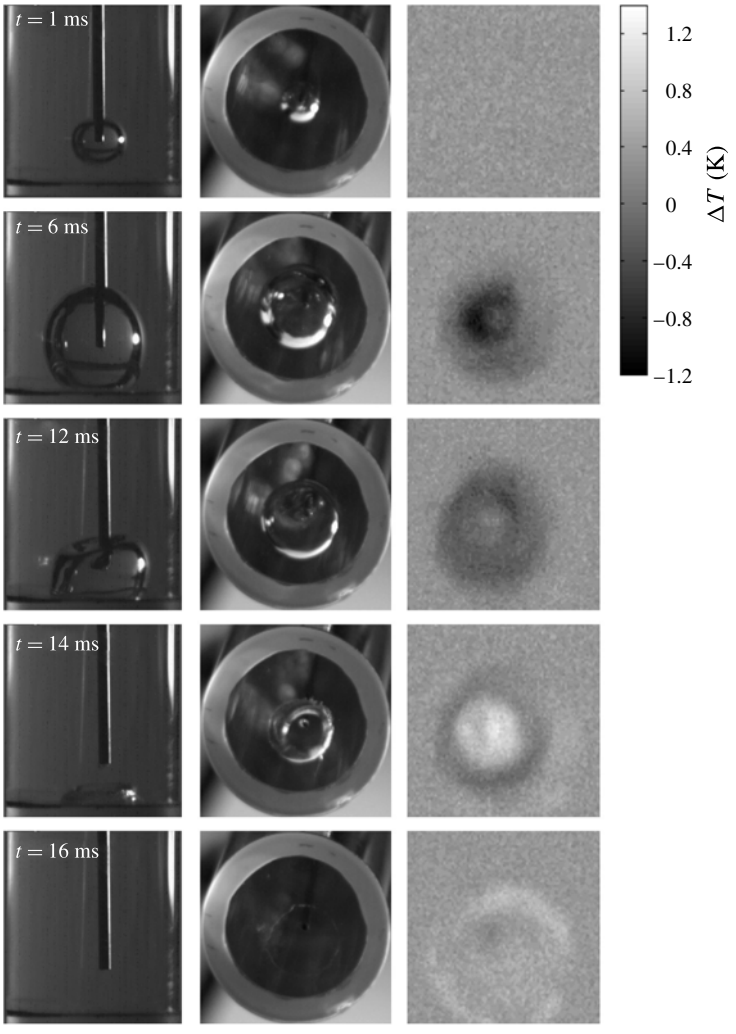

FIGURE 5. Evolutions of the bubble shape and temperature field for the case $\chi = 0.8$.

For a more detailed representation of the thermal effect, vertical cross-sections through the centreline of the images of the temperature fields (like the ones in figures 4–6) were made and put together in a time sequence. This way, one dimension (horizontal one) is 'sacrificed' (one can assume the temperature field to be almost axisymmetric) but a much clearer representation in time is obtained; the diagrams in figure 7 display the temperature variations as a function of time (horizontal axis) and bubble radius (vertical axis) for the three cases.

For $\chi = 0$, the bubble is attached to the observation window right from the start of its growth. It can be observed that the cooler region grows very quickly (in $\sim$3 ms) to its final extent of $\sim$17 mm. The region then slowly shrinks which implies that the collapse is slow. The reason for this peculiar behaviour is the fact that the bubble collapses asymmetrically: the height of the bubble decreases more rapidly than its

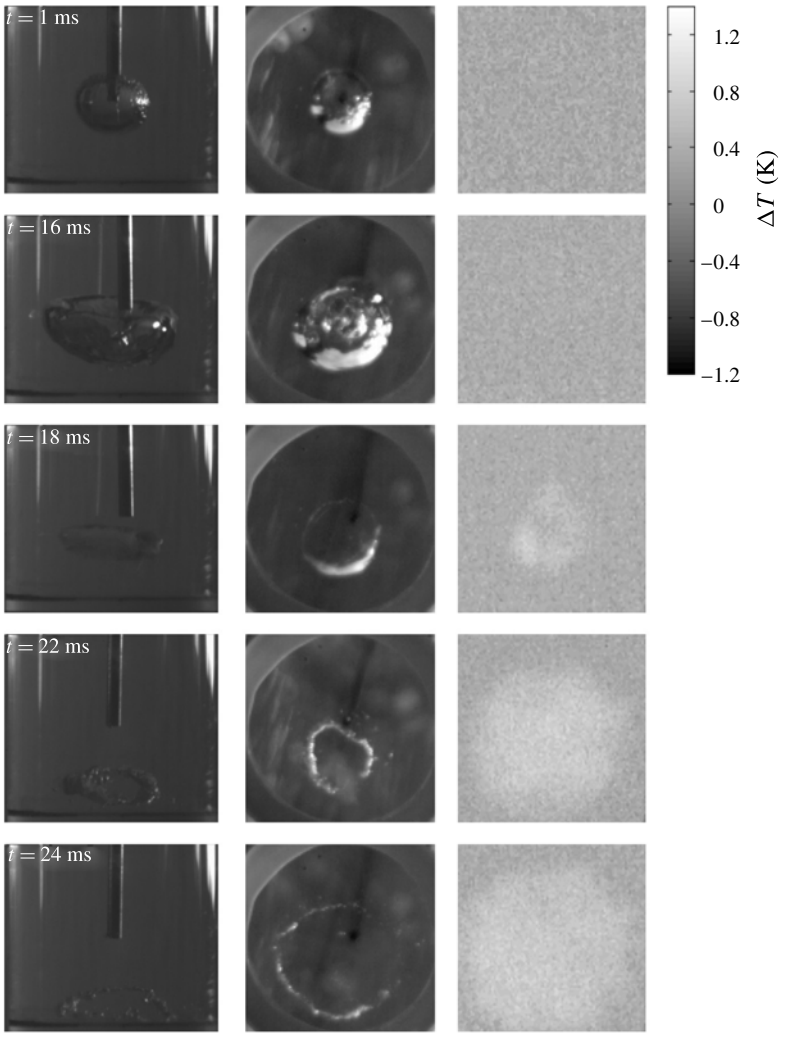

FIGURE 6. Evolutions of the bubble shape and temperature field for the case $\chi = 1.3$.

radius which consequently leads to the formation of a micro-jet. As the jet hits the surface of the window, a rapid and very brief increase of temperature is detected.

The case $\chi = 0.8$ is similar but now the growth phase seems to be longer and the collapse phase shorter. Indeed, due to opacity of the water, the temperature at the bubble interface can be detected only through the part of the bubble that is attached to the wall. As the bubble slowly attaches to the wall, a bigger and bigger part of the bubble interface becomes visible, which results in the detection of a slowly increasing cooler region. The collapse in this configuration has almost the same duration as in the case $\chi = 0$: a very quick change to higher temperatures is recorded at the moment of the micro-jet impact.

In the third case $\chi = 1.3$, the bubble remains unattached to the wall. Therefore, the cooling due to evaporation does not reach the liquid located at the wall, and no temperature variation is detected during this phase. Only the impact of the micro-jet

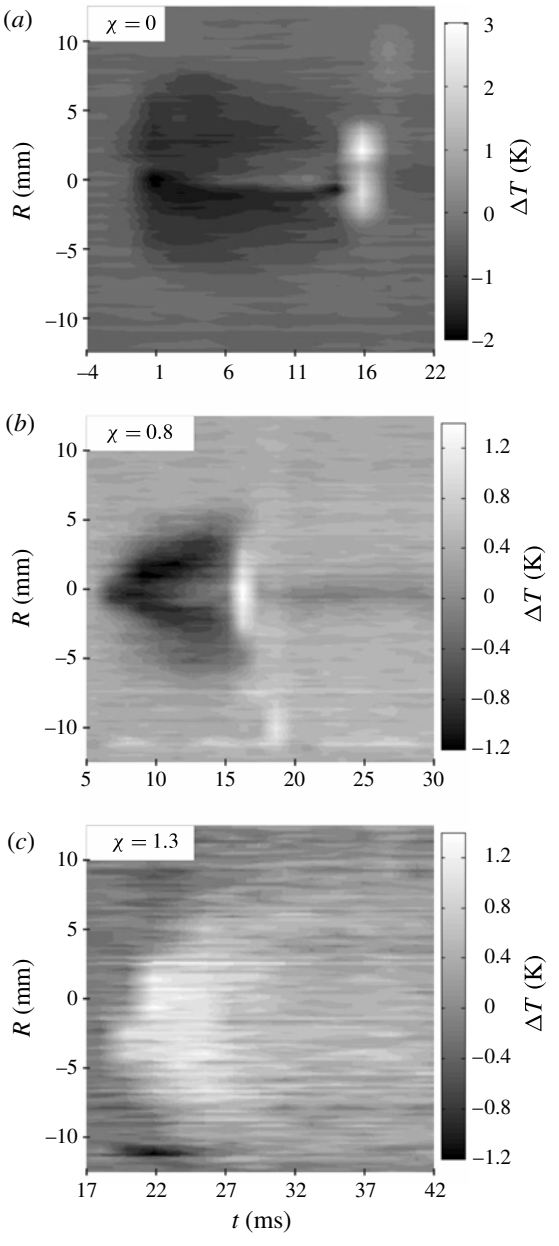

FIGURE 7. Temperature variations over time through vertical cross-sections of the bubble for non-dimensional standoff distances (*a*) $\chi = 0$ (for $t = -4$ to 22 ms), (*b*) $\chi = 0.8$ (for $t = 5$ to 30 ms) and (*c*) $\chi = 1.3$(for $t = 17$ to 42 ms). Bubble growth begins at $t = 0$.

leads, as previously, to a slight increase of the wall temperature. However, it is not as clear as in the previous cases, probably because of the heat diffusion during the distance it travels prior to impact with the wall. Conversely, as already mentioned, the general increase of liquid temperature after the bubble collapse can be clearly observed

in that case: the temperature increase is close to 1 K, compared with the one before the experiment.

In order to more precisely record the temperature evolution and the maximum amplitude of temperature variations in the experiments, the frequency of the camera was increased up to 3840 f.p.s. This setting enabled better temporal resolution of the measurements, but for this we needed to decrease the spatial resolution: the image was reduced to 32×32 pixels which corresponds to a region of $\sim 6 \times 6$ mm only and consequently the recorded temperature fields were practically homogeneous and were treated as such. The results of these measurements are shown and compared to the predictions of the Rayleigh–Plesset and thermal delay theory in the following section.

5.2. *Comparison with simulations by the Rayleigh–Plesset equation combined with the thermal delay theory*

To investigate whether the present experiment corresponds with the theoretical approach presented in §§ 2 and 4, the measured and calculated evolutions of bubble size are first compared. The tube walls and the sapphire observation window certainly influence the bubble dynamics, which is a notable difference with the assumptions involved in the theoretical approach where a bubble in an infinite liquid is assumed.

The determination of the radius evolution in the experiments is based on the estimation of the vapour volume V at each time by image processing. Then, a radius r of a sphere that would accommodate this volume is derived simply from the equation: $r_V = 3V/4\pi)^{1/3}$. Figure 8 shows the evolution of the measured bubble radius r_V compared with that calculated by the Rayleigh–Plesset equation (4.3).

The initial condition for each case can be derived from the pressure drop estimated according to the water hammer equation:

$$\Delta p = \rho_l c_l V_s, \tag{5.1}$$

where Δp is the pressure drop and V_s is the tube velocity just before it is suddenly stopped. Values of velocity in the experiments for cases $\chi = 0$, $\chi = 0.8$ and $\chi = 1.3$ are 0.84, 0.76 and 1.4 m s^{-1}, respectively, as measured optically from the high-speed camera recordings. According to (5.1) these result in $\Delta p = 1.21$, 1.08 and 2.02 MPa, for $\chi = 0$, $\chi = 0.8$ and $\chi = 1.3$, respectively.

Measurements (by a hydrophone Reson TC4013) of the pressure evolution at the bottom of the tube show that the pressure first drops to approximately the negative value of the water hammer pressure. The measured pressure recuperation is, unexpectedly, much slower and a positive pressure pulse is seen only after $\sim$10 ms. We suspect that the slow pressure recovery is related to a very big cavitation bubble which significantly influences both the dynamics of the pressure wave and also the measurements. Since we have no means of determining the real pressure evolution we used a combination of theoretical and measured pressure evolutions for solving the Rayleigh–Plesset equation; there an almost instant pressure drop to the minimum pressure (water hammer pressure) and an almost instant increase to vapour pressure were assumed. The vapour pressure then persisted until the end of the simulation.

The initial bubble radius was the same as observed in the experiment $R_0 = 0.5$ mm. These values are used to obtain numerically the bubble radius evolution in figure 8. It is interesting to observe that even during the bubble collapse, where the bubble was not spherical, the measured and calculated bubble radii fit almost perfectly.

The diagram at a non-dimensional standoff distance $\chi = 0.8$ shows the evolution of the bubble radius for four different bubbles; since the differences are insignificant one can consider the tests to be repeatable.

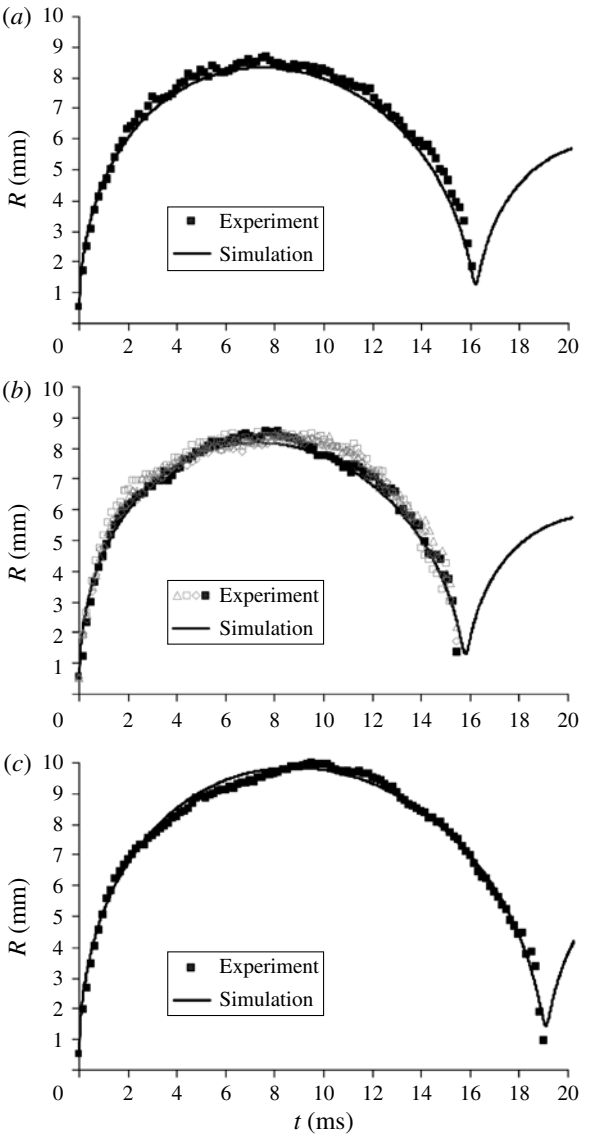

FIGURE 8. Measured and calculated (for a spherical bubble) bubble radius as a function of time for non-dimensional standoff distances (*a*) $\chi = 0$, (*b*) $\chi = 0.8$ (The grey symbols show results from several tests – it can be seen that the experiment is highly repeatable.) and (*c*) $\chi = 1.3$.

It can be observed that the calculation also predicted a rebound of the bubble; this was also seen in the experiments, but the vapour volume could not be estimated with acceptable uncertainty. Moreover, the temperature variations could not be recorded after the collapse of the initial bubble, because of the opacity of the water in the IR spectrum, which makes the study of the rebound of little interest in the context of the present work.

Diagrams displayed in figure 9 show the comparison between the experimentally measured and calculated temperature evolution. A fair agreement between the model

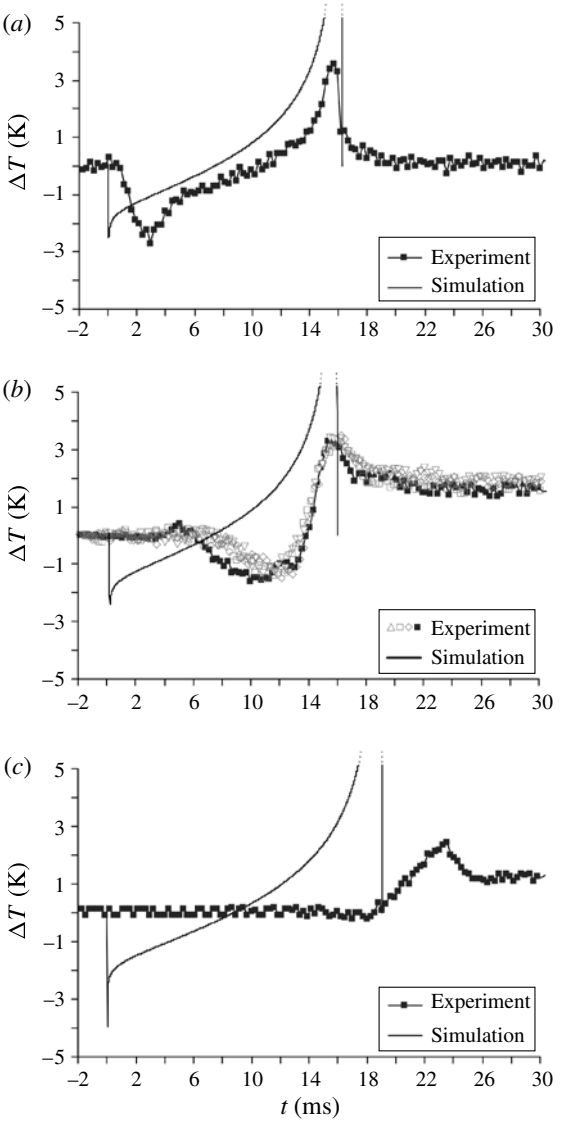

FIGURE 9. Measured and calculated (for a spherical bubble) temperature as a function of time for non-dimensional standoff distances (*a*) $\chi = 0$, (*b*) $\chi = 0.8$ (The grey symbols at show results from several tests – it can be seen that the experiment is highly repeatable.) and (*c*) $\chi = 1.3$.

and the experiments is obtained in the configuration $\chi = 0$. The maximum amplitude of the cooling (∼2 K), at the beginning of the process, is especially well predicted by the Rayleigh–Plesset approach. However, the models predicts an almost instantaneous temperature decrease at $t = 0$, while only a relatively sharp gradient is obtained in the experiment. The temperature evolution after the initial cooling, until the peak due to the bubble collapse at 15 ms, is nicely reproduced by the model, but the amplitude of the peak is not correctly predicted: $\Delta T = 12$ K in the model, while only $\Delta T = 3.6$ K was measured. This may be partially related to the assumption of a spherical bubble,

and also it has been assumed that both bubble evaporation and collapse are triggered by phase change, which is probably valid for the bubble growth, which is slow, but much more questionable for the collapse. Indeed, only the final stage of collapse leads to the very high temperature increase in the vapour phase, and thus to the brief temperature elevation measured at the interface. This is corroborated by the difficulty in detecting experimentally the maximum value of the temperature increase, which has required accelerating the camera speed as much as possible. Consequently, air compression may play a significant role in the bubble size variation, during this final stage of collapse.

For $\chi = 0.8$ the situation is similar, but as the bubble is further from the wall the cooling is not detected immediately in the experiment. It is obtained at $t \approx 5$ ms, i.e. when the bubble contacts the wall (see figure 5). Again, the predicted amplitude of temperature decrease is very close to the measured one. It can also be seen that the temperature increase associated with the final stage of the collapse is predicted to occur at the same time as it was measured, however a much higher amplitude is given by the model. As in figure 8 this diagram also shows the recorded temperature evolutions for the four parallel tests at the same conditions. Again one can conclude that the discrepancies between the test runs are insignificant and that measurements are repeatable.

In configuration at $\chi = 1.3$ only heating can be detected experimentally. It has been suggested in the previous discussion of the results that this temperature increase is obtained when the micro-jet hits the surface of the observation window. The temperature deviation is first detected $\sim$8 ms after the micro-jet inception jet (see figures 2, 6 and 9). This corresponds well to the time it takes the jet to travel the distance of $l = 2\,\chi\,R_{max} \approx 24$ mm from the top point of the bubble (jet inception point) to the wall (the jet velocity was estimated from several consecutive images and is roughly 3 m s^{-1}).

6. Discussion

The results displayed in figure 9 reveal that the liquid heating observed during the bubble collapse is of higher amplitude than the cooling measured during the bubble growth. This point may be related to the abrupt character of the final phase of the bubble collapse, which generates high levels of temperature and pressure in the gas (Yasui 1997; Storey & Szeri 2000). Such a high temperature, of the order of thousands Kelvin, induces heat exchange by conduction with the surrounding liquid, which results in a significant temperature rise at the interface, in addition to that due to vapour condensation. Results obtained in the present experiments suggest that conduction at the bubble interface counterbalances the fact that part of the vapour contained in the bubble does not condense during the collapse, because of the very high speed of bubble compression at the final stage of the process. This phenomenon, which has been investigated by several authors (for example Storey & Szeri 2000; Akhatov *et al.* 2001) is due to the fact that the vapour located at the centre of the bubble does not have a sufficient time to diffuse towards the bubble surface, so some vapour is trapped inside the bubble during the most violent stage of the collapse.

Results also suggest that the bubble growth is not caused by vapourization only. Indeed, the case $\chi = 0$ in figure 9 shows a period of temperature stagnation at the beginning of the bubble expansion (in the first image taken by the IR camera no temperature difference was measured approximately between $t = 0$ and $t = 0.25$ ms), before the liquid cooling is observed. This implies that at the initial stage of bubble growth, the high velocity at the interface (see figure 8) does not allow the

vapourization to occur. To investigate this point, the characteristic time scale of bubble growth τ_{bubble} can be compared to the time scale related to phase change τ_{PC}, as proposed by Storey & Szeri (2000):

$$\tau_{bubble} = \frac{R}{\dot{R}} \tag{6.1}$$

and

$$\tau_{PC} = \frac{R}{\sigma}\sqrt{\frac{2\pi M_{vapour}}{9R_{gas}T_i}}, \tag{6.2}$$

where M_{vapour} is the molecular mass of the vapour, R_{gas} is the constant of perfect gases, and T_i is the temperature at the bubble interface (here we assume the temperature field within the bubble to be homogeneous, hence $T_i = T_b$). The parameter σ is the so-called accommodation coefficient which is included in the expression for the evaporation/condensation flux across the bubble interface, according to the Hertz–Knudsen–Langmuir formula which is derived from the kinetic theory of gases. Detailed expressions for these fluxes can be found for example in Fuster, Hauke & Dopazo (2010). The accommodation coefficient represents a resistance to evaporation or condensation at the interface during the bubble evolution. Although there is no general consensus regarding this parameter, $\sigma = 0.4$ is generally used in most of the recent studies (Yasui 1997; Storey & Szeri 2000, 2001)).

If we consider the initial stage of the bubble growth, i.e. the first 250 μs mentioned previously, the order of magnitude of the bubble radius and the bubble growth velocity can be estimated from figure 8 as $R = 1.7$ mm and $\dot{R} \approx 7$ m s^{-1}, respectively. This leads to $\tau_{bubble} = 2.5 \times 10^{-4}$ s, while $\tau_{PC} = 3.1 \times 10^{-4}$ s is obtained with $\sigma = 0.4$, $T_b = 293$ K, and $R_{gas} = 8.31$ J mol^{-1} K^{-1}. These orders of magnitude of the time scales confirm that vapourization may have insufficient time to occur during the initial stage of bubble growth, which means that the bubble velocity is mainly due to air expansion. It explains why no water cooling is detected by the thermal camera during the first 50 μs of the process.

Later in the sequence, for example at $t = 2$ ms, the bubble radius reaches $R \approx 6$ mm and the bubble velocity decreases to $\dot{R} \approx 1$ m s^{-1}, which leads to characteristic time scales $\tau_{bubble} = 6 \times 10^{-3}$ s and $\tau_{PC} = 10^{-3}$ s. At this point, τ_{bubble} has become significantly higher than τ_{PC}, so the bubble growth is essentially driven by vapourization, which is consistent with the cooling $\Delta T = 3$ K detected by the camera (see figure 9).

A similar phenomenon is expected at the end of the bubble lifetime, during the last abrupt phase of the bubble implosion. Similar velocities as in the initial stages of bubble growth can be observed, hence similar time scales τ_{bubble} and τ_{PC} are obtained. However, no evidence of the time delay can be seen from the thermal measurements, because, as mentioned previously, high levels of temperature within the bubble during this final step of the process also contribute to the heating of the surrounding liquid, so the temperature increase at the wall is observed even if vapour condensation is of minor importance at the end of the process.

One can see that in cases $\chi = 0$ and $\chi = 0.8$ (figures 4, 5 and 9) the liquid temperature starts to increase above the initial level at about $t \approx 14$ ms, which is significantly later than the beginning of the bubble collapse ($t \approx 10$ ms). In both cases the bubble touches the surface of the glass at this stage, so the thermal boundary layer in the liquid due to heat exchanges with the gas should be immediately visible with the thermal camera. This suggests that the temperature increase detected by the camera

is an effect of the large heating of the air inside the bubble, due to its compression during the second part of the collapse; at the very end of the collapse the temperature difference in the boundary layer is mainly due to the conductive heat transferred from the hot inner part of the bubble to the liquid, while the condensation process only slightly affects the liquid temperature.

This is again confirmed by the case $\chi = 1.3$ (figures 6 and 9). In this configuration, the bubble is far from the wall during its implosion, so the increase of the liquid temperature is convected by the re-entrant jet towards the wall (figures 2 and 7). Figure 7 shows that the temperature increase at the wall is spread over a large area, and it is continuously detected between $t = 18$ ms and $t = 24$ ms, i.e. during $T_{heat} \approx 6$ ms. As already mentioned, the velocity of the jet was about $V_{jet} \approx 3$ m s^{-1}. The duration of the high temperature detected at the wall implies that the origin of the re-entrant jet temperature increase has a vertical size that can be roughly estimated as $H = V_{jet} \times T_{heat} = 18$ mm, which is of the order of magnitude of the bubble diameter and much larger than the thickness of the thermal boundary layer on the bubble wall. This shows that the heat convected by the re-entrant jet is not due to the convection of the thermal boundary layer around the bubble but due to the heat conduction of the jet flow as it penetrates the bubble.

7. Conclusions

In the present study, the first direct measurements of the thermodynamic effect on a single cavitation bubble have been obtained. A non-invasive thermographic method was used to measure temperature fields in the liquid during the growth and collapse of a single cavitation bubble, which was initiated mechanically without the introduction of heat sources.

Results show that during the bubble growth the temperature of the liquid–vapour boundary layer decreases. At the collapse a reversed process was observed as the temperature increased. The contribution of four processes (evaporation, expansion, condensation and compression) was discussed. Based on a comparison of characteristic times of conductive and latent heat flows it was concluded that the two main mechanisms that drive the heat fluxes are evaporation and condensation, while the other two, expansion and compression, contribute significantly only at the very beginning and very end of the bubble lifetime. Consequently, the theory of the so-called ‘thermal delay’ (Brennen 1973), which is based on this assumption, was applied, and it was found that the predicted temperature variations in the liquid are in relatively good agreement with the present measurements. This suggests that the thermal delay theory is valid in the present case for most of the bubble evolution, which is further indirect evidence of the predominance of mass transfers in the bubble evolution. Definite confirmation of the thermal delay theory is beyond the scope of the present work and could possibly be obtained after additional experiments in various other liquids; however the success of such experiments is questionable due to the unique property of water that it is opaque to the infrared spectrum.

Further work will include studies of direct temperature measurements in developed hydrodynamic cavitation with the purpose of improving numerical methods for prediction of cavitation in thermosensible fluids.

Acknowledgement

M.D. would like to thank the European Space Agency (ESA) which enabled the study within the scope of the project ‘Cavitation in Thermosensible Fluids’.

REFERENCES

AKHATOV, I., LINDAU, O., TOPOLNIKOV, A., METTIN, R., VAKHITOVA, N. & LAUTERBORN, W. 2001 Collapse and rebound of a laser-induced cavitation bubble. *Phys. Fluids* **13**, 2805–2819.

BRENNEN, C. E. 1973 The dynamic behavior and compliance of a stream of cavitating bubbles. *Trans. ASME: J. Fluids Engng* **95** (4), 533–541.

BRENNEN, C. E. 1995 *Cavitation and Bubble Dynamics*. Oxford University Press.

CERVONE, A., TESTA, R. & D'AGOSTINO, L. 2005 Thermal effects on cavitation instabilities in helical inducers. *J. Propul. Power* **21**, 893–899.

CHEN, Q.-D. & WANG, L. 2004 Production of large size single transient cavitation bubbles with tube arrest method. *Chin. Phys.* **13** (4), 564–570.

CHEN, Q.-D. & WANG, L. 2005 Luminescence from transient cavitation bubbles in water. *Phys. Lett.* A **339**, 110–117.

CHESTERMAN, W. D. 1952 The dynamics of small transient cavities. *Proc. Phys. Soc.* B **65**, 846–858.

FRANC, J.-P., BOITEL, G., RIONDET, M., JANSON, E., RAMINA, P. & REBATTET, C. 2010 Thermodynamic effect on a cavitating inducer-part II: on-board measurements of temperature depression within leading edge cavities. *Trans. ASME: J. Fluids Engng* **132** (2), 021304.

FRANC, J.-P. & MICHEL, J.-M. 2004 *Fundamentals of Cavitation*. Fluid Mechanics and Its Applications, vol. 76, Springer.

FRANC, J.-P., REBATTET, C. & COUKON, A. 2004 An experimental investigation of thermal effects in a cavitating inducer. *Trans. ASME: J. Fluids Engng* **126**, 716–723.

FRUMAN, D. H., REBOUD, J. L. & STUTZ, B. 1999 Estimation of thermal effects in cavitation of thermosensible liquids. *Intl J. Heat Mass Transfer* **42**, 3195–3204.

FUSTER, D., HAUKE, G. & DOPAZO, C. 2010 Influence of the accommodation coefficient on nonlinear bubble oscillations. *J. Acoust. Soc. Am.* **128** (1), 5–10.

HALE, G. M. & QUERRY, M. R. 1973 Optical constants of water in the 200 nm to 200 μm wavelength region. *Appl. Opt.* **12**, 555–563.

HAUKE, G., FUSTER, D. & DOPAZO, C. 2007 Dynamics of a single cavitating and reacting bubble. *Phys. Rev.* E **75**, 066310.

HORD, J. 1973*a* Cavitation in liquid cryogens II – hydrofoil. *NASA CR*-2156.

HORD, J. 1973*b* Cavitation in liquid cryogens III – ogives. *NASA CR*-2242.

HORD, J., ANDERSON, L. M. & HALL, W. J. 1972 Cavitation in liquid cryogens I – Venturi. *NASA CR*-2054.

KATO, H. 1984 Thermodynamic effect on incipient and development of sheet cavitation. In *Proceedings of International Symposium on Cavitation Inception*, New Orleans, LA, pp. 127–136.

MATULA, T. J., HILMO, P. R., STOREY, B. D. & SZERI, A. J. 2002 Radial response of individual bubbles subjected to shock wave lithotripsy pulses in vitro. *Phys. Fluids* **14**, 913–921.

PHILIPP, A. & LAUTERBORN, W. 1998 Cavitation erosion by single laser-produced bubbles. *J. Fluid Mech.* **361**, 75–116.

PLESSET, M. S. 1949 The dynamics of cavitation bubbles. *J. Appl. Mech.* **16**, 277–282.

PLESSET, M. S. & CHAPMAN, R. B. 1971 Collapse of an initially spherical vapour cavity in the neighborhood of a solid boundary. *J. Fluid Mech.* **47** (2), 283–290.

RUGGERI, R. S. & MOORE, R. D. 1969 Method for prediction of pump cavitation performance for various liquids, liquid temperature, and rotation speeds. *NASA TN* D-5292.

SAROSDY, L. R. & ACOSTA, A. J. 1961 Note on observations of cavitation in different fluids. *Trans. ASME: J. Basic Engng* **83**, 399–400.

SEKITA, R., WATANABEL, A., HIRATA, K. & IMOTO, T. 2001 Lessons learned from H-2 failure and enhancement of H-2a project. *Acta Astron.* **48** (5–12), 431–438.

STAHL, H. A. & STEPANOFF, A. J. 1956 Thermodynamic aspects of cavitation in centrifugal pumps. *Trans. ASME: J. Basic Engng* **78**, 1691–1693.

STEPANOFF, A. J. 1961 Cavitation in centrifugal pumps with liquids other than water. *J. Engng Power* **83**, 79–90.

STOREY, B. D. & SZERI, A. J. 2000 Water vapour, sonoluminescence and sonochemistry. *Proc. R. Soc. Lond.* A **456**, 1685–1709.

STOREY, B. D. & SZERI, A. J. 2001 A reduced model of cavitation physics for use in sonochemistry. *Proc. R. Soc. Lond.* A. **457**, 1685–1700.

SZERI, A. J., STOREY, B. D., PEARSON, A. & BLAKE, J. R. 2003 Heat and mass transfer during the violent collapse of nonspherical bubbles. *Phys. Fluids* **15**, 2576–2586.

TOEGEL, R., GOMPF, B., PECHA, R. & LOHSE, D. 2000 Does water vapour prevent upscaling sonoluminescence? *Phys. Rev. Lett.* **85**, 3165–3168.

TONG, R. P., SCHIFFERS, W. P., SHAW, J. S., BLAKE, J. R. & EMMONY, D. C. 1999 The role of splashing in the collapse of the laser-generated cavity near a rigid boundary. *J. Fluid Mech.* **380**, 339–361.

WATANABE, S., HIDAKA, T., HORIGUCHI, H., FURUKAWA, A. & TSUJIMOTO, Y. 2007 Steady analysis of the thermodynamic effect of partial cavitation using the singularity method. *Trans. ASME: J. Fluids Engng* **129** (2), 121–127.

YASUI, K. 1997 Alternative model of single-bubble sonoluminescence. *Phys. Rev.* E **56**, 6750–6760.